

Size-differentiated Export Flux in Different Dynamical Regimes in the Ocean

Mathieu Dever¹, D Nicholson², M M Omand³, and A Mahadevan²

¹Wood Hole Oceanographic Institution

²Woods Hole Oceanographic Institution

³University of Rhode Island

November 21, 2022

Abstract

Export of Particulate Organic Carbon (POC) is mainly driven by gravitational sinking. Thus, traditionally, it is thought that larger, faster-sinking particles make up most of the POC export flux. However, this need not be the case for particles whose sinking speeds are comparable to the vertical velocities of a dynamic flow field that can influence the descent rate of particles. Particles with different settling speeds are released in two process-oriented model simulations of an upper ocean eddying flow in the Northeast Pacific to evaluate the impact of (1) ocean dynamics on the respective contribution of the different sinking-velocity classes to POC export, and (2) the particle number size-spectrum slope. The analysis reveals that the leading export mechanism changes from gravitationally-driven to advectively-driven as submesoscale dynamics become more active in the region. The vertical velocity associated with submesoscale dynamics enhances the contribution of slower-sinking particles to POC export flux by a factor ranging from 3 to 10, especially where the relative abundance of small particles is large, (i.e., steep particle size-spectrum slope). Remineralization generally decreases the total amount of biomass exported, but its impact is weaker in dynamical regimes where submesoscale dynamics are present and export is advectively-driven.

Size-differentiated Export Flux in Different Dynamical Regimes in the Ocean

M. Dever¹, D. Nicholson¹, M. M. Omand², and A. Mahadevan¹

¹Woods Hole Oceanographic Institution, Woods Hole, MA 02543, USA

²Graduate School of Oceanography, University of Rhode Island, Narragansett, Rhode Island, USA

Key Points:

- Submesoscale dynamics enhance the contribution of slow-sinking particles to POC export, especially for steep particle size-spectrum slopes
- Remineralization processes intensify the role of slow-sinking particles, to the point where these particles sometimes dominate POC export

Corresponding author: Mathieu Dever, mdever@whoi.edu

Abstract

Export of Particulate Organic Carbon (POC) is mainly driven by gravitational sinking. Thus, traditionally, it is thought that larger, faster-sinking particles make up most of the POC export flux. However, this need not be the case for particles whose sinking speeds are comparable to the vertical velocities of a dynamic flow field that can influence the descent rate of particles. Particles with different settling speeds are released in two process-oriented model simulations of an upper ocean eddying flow in the Northeast Pacific to evaluate the impact of (1) ocean dynamics on the respective contribution of the different sinking-velocity classes to POC export, and (2) the particle number size-spectrum slope. The analysis reveals that the leading export mechanism changes from gravitationally-driven to advectively-driven as submesoscale dynamics become more active in the region. The vertical velocity associated with submesoscale dynamics enhances the contribution of slower-sinking particles to POC export flux by a factor ranging from 3 to 10, especially where the relative abundance of small particles is large, (i.e., steep particle size-spectrum slope). Remineralization generally decreases the total amount of biomass exported, but its impact is weaker in dynamical regimes where submesoscale dynamics are present and export is advectively-driven. In an advectively-driven export regime, remineralization processes counter-intuitively enhance the role of slower-sinking particles to the point where these slower-sinking velocity classes dominate the export, therefore challenging the traditional paradigm for POC export. This study demonstrates that slow-sinking particles can be a significant contribution, and at times, even dominate the export flux.

1 Introduction

Photosynthesis in the sunlit upper ocean and the production of Particulate Organic Carbon (POC) takes up dissolved inorganic carbon and facilitates the uptake of CO_2 from the atmosphere. The sinking of POC exports organic carbon from the upper ocean to the interior, leading to the sequestration of carbon (Falkowski et al., 1998) on timescales ranging from days to years depending on the sinking depth and circulation. Despite progress on sampling and viewing particles in the ocean, direct measurements of particles sinking velocities are difficult to obtain, and often inferred from key parameters such as particle type, size, and density (McDonnell & Buesseler, 2010; McDonnell & Buesseler, 2012).

Traditionally, POC export is thought to occur through gravitational sinking and one-dimensional models have been used to describe the sinking POC flux with depth (Jackson et al., 1997; Armstrong et al., 2001; DeVries et al., 2014; Omand et al., 2020). Particles produced through primary and secondary production in the surface layer that are relatively large and fast sinking tend to sink out of the upper surface layer on timescales shorter than the timescale on which the particles get remineralized. It is reasonable to treat POC export as sinking-dominated if the vertical advective velocities in the ocean are weaker than the velocities associated with gravitational sinking. However, Particulate Organic Matter (POM) has a wide range of particle shape, size and type, that result in particle sinking velocities ranging from practically zero, to several hundreds of meters per day (Riley et al., 2012; Baker et al., 2017). The size spectrum, or number distribution of particle sizes, is usually characterized by a power law with the power ranging between -2 and -4, for which the abundance of small particles is $\mathcal{O}(10^4 - 10^8)$ greater than large particles (McCave, 1984; Petrik et al., 2013). The biomass size spectrum, which indicates the distribution of biomass vs. particle size, tends to be flatter and variable in shape (Sheldon et al., 1972) compared to the particle number spectrum, because the volume (and mass) of a particle scales with its linear size raised to a power that exceeds 1 (and typically varies between 2 and 3 depending on shape and porosity). Importantly, it means that a significant fraction of the particulate biomass is in the small size fraction (Richardson & Jackson,

2007). Even though the sinking velocity w_s of particles does not perfectly relate to particle size l , it is fair to assume that $w_s \sim l^n$ (with $n = 2$ according to Stokes law, and $1 < n < 2$ for complex particle shapes). Due to this, as well as the fact that particles of organic matter are not very much greater in their densities than seawater, a significant fraction of the biomass sinks very slowly (at velocities less than tens of meters per day). When the gravitational sinking velocity of particles is comparable to (or smaller than) the vertical velocities in the flow field, the dynamics of the flow field can impact the trajectories and fate of the POC. Thus, depending on the flow dynamics, and the fraction of slow-sinking particulate biomass, the sinking of organic matter can be affected by the fluid flow in the ocean.

Recent studies have shown that ocean dynamics can play a role in driving the transport of carbon from the euphotic layer to the ocean interior. For example, enhanced vertical velocities along the edge of a mesoscale eddy led to a funneling of particles along the eddy's periphery (van Haren et al., 2006; Waite et al., 2016) and in mesoscale features in the California current (Stukel et al., 2017). Omand et al. (2015) found that submesoscale mixed layer eddies, while contributing to the restratification of a frontal zone, were subducting a large amount of non-sinking POC from the surface productive layer during the onset of the Spring bloom in the subpolar North Atlantic. Advectively subducting plumes or filaments of high oxygen, chlorophyll and small POC (evidenced through backscatter) were detected from a suite of gliders during the North Atlantic Bloom experiment (Alkire et al., 2012). Using model simulations to capture the process of eddy-driven subduction, Omand et al. (2015) estimated the downward advective flux of non-sinking POC and parameterized it. Briggs et al. (2011) quantified the flux of fast-sinking particles consisting largely of diatoms from observations of optical backscatter. But, these estimates did not account for a range of sinking particle velocities. Typically, POM has a wide spectrum of sinking velocities and in order to understand its fate and export, we need to consider the biomass distribution as a function of the particle sinking velocity spectrum and its interaction with the dynamics of the flow field in the ocean.

A growing body of literature focusing on submesoscale (1-10 km) dynamics is exploring its impact on biogeochemical processes (Lévy et al., 2012; Mahadevan, 2016). Submesoscale dynamics, characterized by Rossby numbers of order 1, typically develop in filaments in areas where sharp density fronts exist (Thomas, Taylor, et al., 2013; Klein & Lapeyre, 2009; McWilliams, 2016). In this dynamical regime, geostrophic balance breaks down and a secondary ageostrophic circulation develops across the front, capable of generating large vertical velocities on the order of 100 m/day (Fox-Kemper et al., 2008; Mahadevan, 2016). On the denser side of the front, the vorticity is cyclonic and associated with downwelling velocities, while anticyclonic vorticity and upwelling is expected on the lighter side of the front. The distribution of relative vorticity associated with submesoscale dynamics near the surface exhibits an asymmetry with higher values of positive vorticity than negative vorticity (Rudnick, 2001), leading to more localized and more intense downwelling regions, as opposed to weaker and larger scale upwelling regions (Mahadevan & Tandon, 2006). Enhanced vertical velocities can aid the supply nutrients to the sunlit layer of the ocean for primary production (Mahadevan & Archer, 2000; Lévy et al., 2001) or can significantly increase the export of POC to the ocean interior through localized downwelling (Lévy et al., 2012; Gruber et al., 2011; Estapa et al., 2015; Omand et al., 2015). The downwelling velocities $\mathcal{O}(100$ m/day) generated at submeso-scales provide a physical mechanism for exporting slow sinking or neutrally buoyant particles on timescales shorter than their remineralization timescales. If the fraction of biomass associated with such slow sinking velocities is significant, submesoscale dynamics can potentially impact the export of POC.

We rely on a submesoscale-resolving, non-hydrostatic ocean model to simulate the dynamics in the upper few hundred meters of the ocean. The dynamical model is

116 coupled with a particle-tracking module to model the advection of particles by fluid
 117 flow, while neglecting the effects of particle inertia and drag on their advection. In
 118 addition, the particles sink with a range of sinking velocities (between 0.025–5 m
 119 day⁻¹) that is based on the range of vertical currents modeled in this region. We
 120 aim to address the transitional regime of the particle sinking velocity spectrum, where
 121 both advection and sinking speeds have similar order of magnitudes. A similar study
 122 with sinking tracers showed the influence of the flow (Taylor et al., 2020), but the use
 123 of particles enables a characterization of export associated with each sinking class of
 124 particles.

125 The model is used to quantify the contribution of slow-sinking particles to carbon
 126 export, as a function of (1) the dynamics of the flow field, (2) the slope of the sinking
 127 velocity spectrum, and (3) the remineralization timescale. Particles in the model
 128 are prescribed with both a constant and time-varying sinking velocity to mimic a
 129 remineralizing behavior. Particles are released in two fundamentally different flow
 130 fields in terms of dynamics based on observed conditions in the Northeast Pacific:
 131 In the summer, where ocean dynamics are characterized by low Rossby numbers and
 132 weak vertical advective velocities, and in the winter, where ocean dynamics include
 133 submesoscale frontal structures and local Rossby numbers $\mathcal{O}(1)$. Both simulations
 134 and the particle-tracking module are described in Section 2. The impact of particles
 135 characteristics and ocean dynamics on the export of POC is quantified in Section 3,
 136 and discussed in Section 4. Section 5 summarizes the key conclusions of the study.

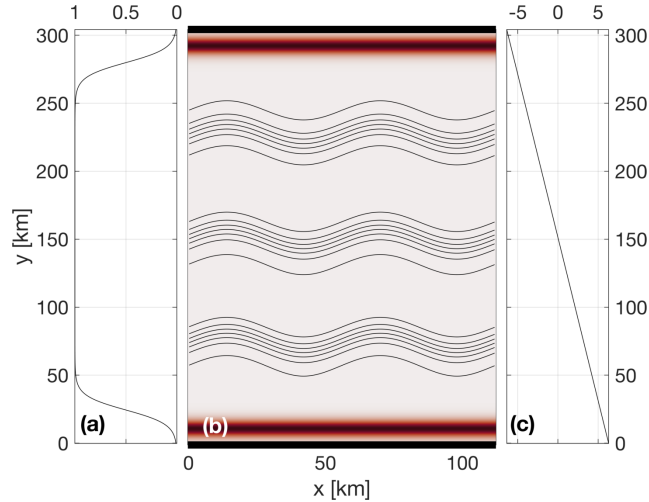
137 2 Methods

138 2.1 Model setup and domain

139 This study uses a non-hydrostatic, three-dimensional, Process Study Ocean Model
 140 (PSOM; Mahadevan et al., 1996b, 1996a) to simulate an eddy field that is represen-
 141 tative of the Northeast Pacific Ocean. The model is set in a channel configuration
 142 with periodic east-west boundaries, and solid boundaries in the south and north. The
 143 domain covers 112 km in the x-direction, 304 km in the y-direction, and 1000 m in
 144 the vertical (Figure 1). The horizontal resolution is 500 m, while a stretched grid is
 145 used in the vertical with 32 levels ranging in thickness from 1.25 m near the surface to
 146 70 m at the lowermost level. The model is integrated numerically in time and evolves
 147 the temperature, salinity, free-surface height, pressure, and three-dimensional velocity
 148 field from an initial state, subject to momentum and buoyancy fluxes applied through
 149 the surface boundary.

157 Time-varying wind stress and heat flux are prescribed at the surface boundary.
 158 Time series are computed from measurements collected at Station Papa and available
 159 through the Pacific Marine Environmental Laboratory (PMEL, 2018). Daily wind
 160 stress and net heat fluxes are calculated over the period 2007-2016 to produce a year-
 161 long climatology. A squared low-pass filter with a cut-off frequency of 8.5 days is
 162 applied to both time series to remove high-frequency variability. In all numerical
 163 experiments, simulations are run for the first 5 days without any forcing applied to
 164 the surface boundary. Surface wind stress and heat fluxes are then linearly ramped up
 165 between days 5 and 10 of the simulation, to reach realistic values at day 10.

166 While the meridional component, τ_y , is set to zero, the zonal component of
 167 the wind stress, τ_x , is prescribed at the surface throughout the model domain and
 168 is tapered at the northern and southern boundaries to avoid excessive Ekman-driven
 169 upwelling and downwelling (Figure 1a). A restoration timescale is prescribed to contain
 170 the curl-driven upwelling and downwelling regions generated by the tapering of the
 171 wind stress, as well as to limit internal wave reflection at the solid boundaries back
 172 into the domain (Figure 1b). While net surface heat fluxes are homogeneous in the



150 **Figure 1.** PSOM model setup. (a) Meridional profile of scaling coefficient that multiplies the
 151 time-varying zonal wind stress τ_x shown in Fig. 3a. The taper at north and south boundaries
 152 prevents ‘coastal’ up-/down-welling being entirely concentrated in the boundary grid cell. (b)
 153 Restoration factor (color shading) used to dampen internal wave reflection at boundaries as well
 154 as up-/down-welling due to the windstress curl. Surface density contours (black) show the three
 155 fronts used to initialize the model. (c) Meridional variation of the time-dependent surface heat
 156 flux (Fig. 3a) prescribed over the domain.

173 zonal direction, a meridional gradient is maintained throughout the simulation. The
 174 meridional gradient was determined from the North American Regional Reanalysis
 175 (NARR) product (Mesinger et al., 2006), and set to $1/24$ W/m²/km (Figure 1c).

176 Initial hydrographic conditions are determined from a three-dimensional gridded
 177 field of temperature and salinity from Argo floats (Gaillard, 2015; Gaillard et al., 2016).
 178 Argo data is averaged monthly over the period 2002-2012 and two different months are
 179 used to initialize the two main numerical experiments for this study: Climatological
 180 conditions in April are used to initialize the *Papa_summer* experiment, while January
 181 climatological conditions are used to initialize the *Papa_winter* experiment (Table 1).
 182 The north-south background density gradient is then intensified into three fronts lo-
 183 cated at $y = 75$, $y = 150$, and $y = 225$ km (Figure 1). The amplitude of the density
 184 gradient associated with the three fronts is determined from the probability distribu-
 185 tion function (PDF) of the density gradients measured by underwater gliders deployed
 186 around Station Papa over the period 2008-2010 (Pelland et al., 2016; Pelland, 2018).
 187 To reduce model spin-up time, density fronts are perturbed by a sinusoidal wave with
 188 a wavelength close to the 1st baroclinic deformation radius ($\lambda = 66$ km). Similar
 189 PSOM configurations were successfully used in previous studies (Mahadevan et al.,
 190 2012; Omand et al., 2015). The model does not simulate surface waves or boundary
 191 layer turbulence, but rather, examines the fate of particulate organic matter beneath
 192 the turbulent surface boundary layer.

193 Two main experiments are conducted using the same configuration of PSOM,
 194 where only initial conditions and surface forcings are varied: *Papa_summer* aims at
 195 generating ocean dynamics representing conditions in the Northeast Pacific in the sum-
 196 mertime. Summer ocean dynamics are characterized by a flow generally in geostrophic
 197 balance, with relatively weak density gradients and low Rossby numbers ($Ro \ll 1$).
 198 *Papa_winter* aims at capturing wintertime ocean conditions in the region. A different

217 **Table 1.** Summary of the key characteristics of PSOM experiments *Papa_summer* and
 218 *Papa_winter*.

	<i>Papa_summer</i>	<i>Papa_winter</i>
Time period	April – July	January – March
Spin-up	60 days	50 days
Advective timestep	216 s	108 s
Horizontal diffusivity	$1 \text{ m}^2 \text{ s}^{-1}$	$0.2 \text{ m}^2 \text{ s}^{-1}$
Restoration timescale	3 days	15 days
Zonal wind stress	$0 - +0.16 \text{ N m}^{-2}$	$-0.05 - +0.17 \text{ N m}^{-2}$
Surface heat flux	$-46.8 - +167.5 \text{ W m}^{-2}$	$-57.6 - +15.3 \text{ W m}^{-2}$
Maximum M^2 ($\times 10^{-8}$)		
initial	3.2 s^{-2}	33.9 s^{-2}
spun-up	12.0 s^{-2}	50.0 s^{-2}
Maximum N^2 ($\times 10^{-4}$)		
initial	1.5 s^{-2}	1.6 s^{-2}
spun-up	3.1 s^{-2}	1.1 s^{-2}
Averaged mixed layer depth		
initial	73 m	85 m
spun-up	11 m	93 m

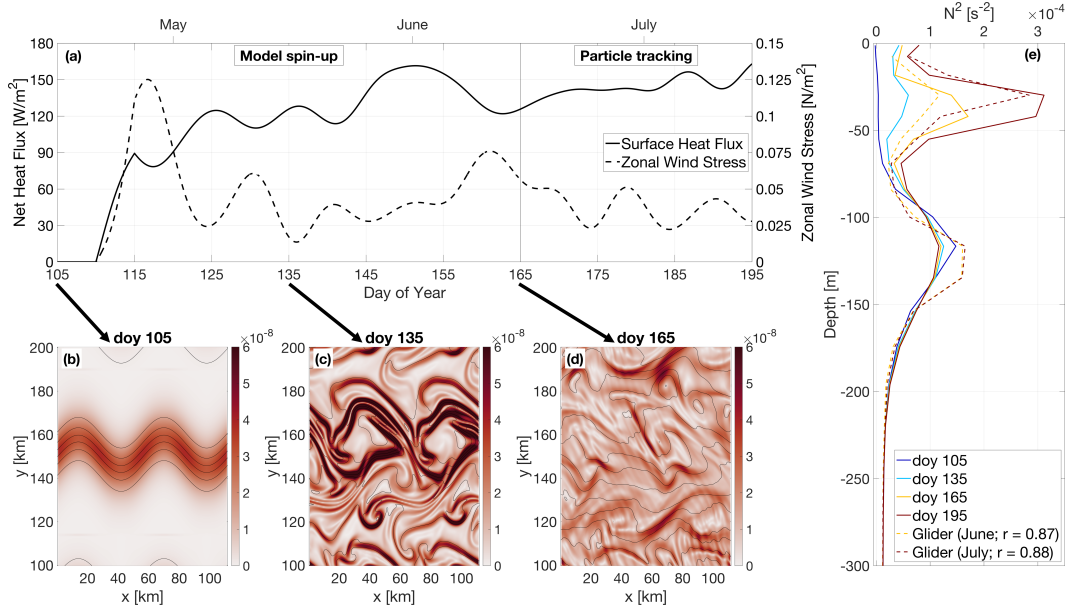
199 dynamical regime is expected to dominate during wintertime when mixed layers are
 200 deeper and lateral density gradients enhanced, with sharper density fronts, filament-
 201 like features and localized Rossby number $Ro = \mathcal{O}(1)$ over spatial scales $\mathcal{O}(1 \text{ km})$
 202 (Mensa et al., 2013; Callies et al., 2015; Thompson et al., 2016). The individual
 203 characteristics of each of *Papa_summer* and *Papa_winter* are detailed below.

204 **2.1.1 *Papa_summer* Model Experiment**

205 In *Papa_summer*, PSOM is initialized based on climatological Argo data in April.
 206 The magnitude of the density gradient across the front is set to $3.34 \times 10^{-6} \text{ kg/m}^3/\text{m}$,
 207 which corresponds to the 95th percentile of the PDF of density gradients measured
 208 in April from glider data collected in the region (Figure 2 and Table 1). The model
 209 is run with a timestep of 216 s and is allowed to spin-up for 60 days, allowing sum-
 210 mer stratification to develop. The model is then run for 30 additional days, saving
 211 instantaneous model fields every 3 hours for particle tracking. The month of April
 212 is chosen for initialization so the experiment would capture the onset of positive net
 213 heat fluxes, and the summer restratification that ensues in July-August (Figure 2). In
 214 this region, the summer stratification is associated with large primary productivity,
 215 particle production, and POC export (e.g., fecal pellets, dead phytoplankton; Plant
 216 et al., 2016).

228 **2.1.2 *Papa_winter* Model Experiment**

229 In *Papa_winter*, PSOM is initialized based on climatological Argo data in Janu-
 230 ary. The frontal gradient is set to $3.54 \times 10^{-5} \text{ kg/m}^3/\text{m}$, which corresponds to the
 231 99th percentile of the PDF of density gradients measured in January from glider data
 232 collected in the region (Figure 3 and Table 1). The model is allowed to spin-up for 50
 233 days allowing for the prescribed fronts to become unstable. To accommodate for the
 234 larger density gradients and stronger velocities, the advective timestep is shortened to
 235 108 s and the horizontal diffusivity is lowered to $0.2 \text{ m}^2/\text{s}$ throughout the experiment.
 236 The model is run for 30 additional days, saving instantaneous model fields every 1.5

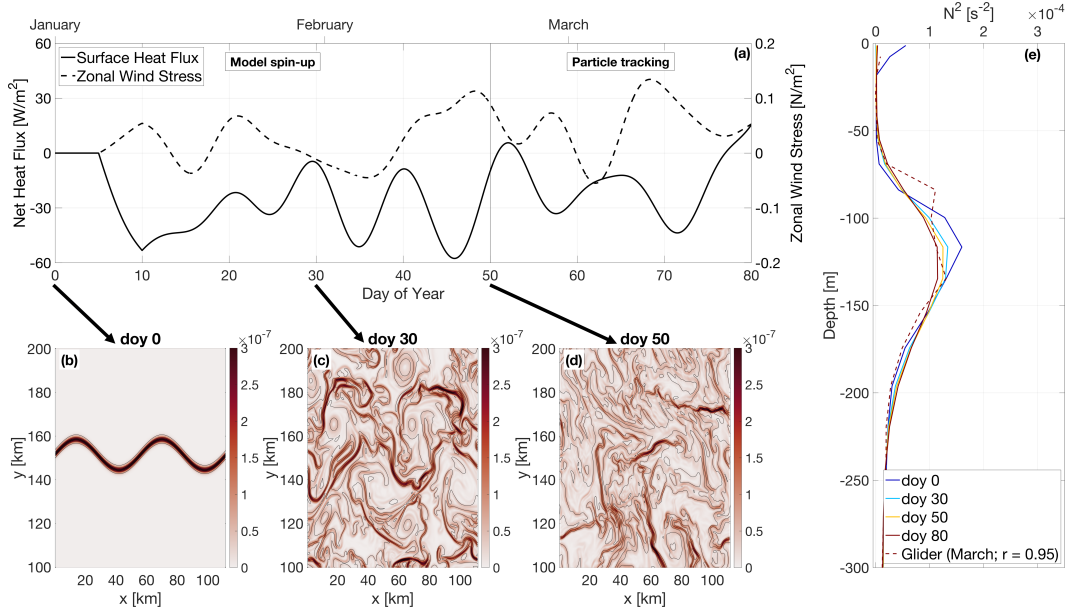


219 **Figure 2.** PSOM configuration for *Papa_summer*. (a) Time series of net heat fluxes and wind
 220 stress prescribed at the surface. Notice the positive heat fluxes, as well as downfront winds (i.e.
 221 eastward) persisting throughout the experiment. (b)-(d) surface horizontal buoyancy gradients
 222 $M^2 = |\nabla_H b|^2$ (in s^{-2}) at day of year (doy) 105, 135, and 165. Black contours show isopycnals (in
 223 kg/m^3 ; $\text{CI} = 0.01 \text{ kg}/\text{m}^3$). (e) Vertical profile of the buoyancy frequency N^2 at day of year 105,
 224 135, 165, and 195, showing the development of summer stratification centered at $z = 30 \text{ m}$ (solid
 225 lines). Monthly-average vertical stratification obtained from glider profiles collected in June and
 226 July are superimposed (dashed lines), along with the correlation coefficient between observations
 227 and model outputs.

237 hours for particle tracking. The month of January is chosen for initialization so the
 238 experiment would capture the time of year where the mixed layer is the deepest, and
 239 Rossby number $O(1)$ occur more frequently. The objective is for this experiment to
 240 contrast *Papa_summer* by capturing the statistics of ocean conditions dominated by
 241 submesoscale dynamics.

250 2.1.3 Validation

251 To ensure that PSOM simulations yielded realistic conditions for both *Papa_summer*
 252 and *Papa_winter*, distributions of horizontal (M^2) and vertical (N^2) buoyancy gradi-
 253 ents are compared with glider observations collected over the period 2008-2009 (Pelland
 254 et al., 2016). During this period, underwater gliders sampled in a “bow-tie” pattern
 255 centered on Station Papa. Gliders sample the water column in a triangular wave
 256 pattern, whose shape is easily affected by currents, due to the slow moving speed of
 257 the glider ($\sim 1 \text{ km}/\text{hr}$). It is therefore challenging to associate a specific spatial scale
 258 with gradients computed between glider profiles, as profile separation distances can be
 259 highly variable through depth and time. To circumvent this issue, horizontal buoy-
 260 ancy gradients are computed between each pair of glider profiles available within one
 261 branch of the bow-tie. Each along-track lateral buoyancy gradient is thus associated
 262 with a specific separation scale and a timestamp. Glider-based density gradients can
 263 be affected by internal waves. To filter the impact of internal waves on the PDF of
 264 horizontal buoyancy gradients, only gradients computed at a scale of twice the Rossby



242 **Figure 3.** PSOM configuration for *Papa_winter*. (a) time series of net heat fluxes and wind
 243 stress prescribed at the surface. Notice the mostly negative heat fluxes, as well as alternating
 244 zonal wind direction. (b)-(d) surface horizontal buoyancy gradients $M^2 = |\nabla_H b|^2$ (in s^{-2}) at day
 245 of year (doy) 0, 30, and 50. Black contours show isopycnals (in kg/m^3 ; $\text{CI} = 0.01 \text{ kg}/\text{m}^3$). (e)
 246 Vertical profile of the buoyancy frequency N^2 at day 0, 30, 50, and 80, showing the persistence
 247 of the halocline between $z = 80$ and $z = 180$ m throughout the experiment (solid lines). Monthly-
 248 average vertical stratification obtained from glider profiles collected in March is superimposed
 249 (dashed line), along with the correlation coefficient between observations and model outputs.

265 radius ± 1 km are considered. Rossby radii are estimated from the glider data and
 266 are ~ 8 km in winter and ~ 20 km in summer.

267 2.2 Particle Tracking Experiments

268 2.2.1 Particle Advective Scheme

To quantify the impact of submesoscale dynamics on the export of Particulate Organic Matter (POC), Lagrangian particle trajectories are computed using the same scheme as in “TRACMASS” (Döös et al., 2013) with the flow fields from the two experiments described above. The three-dimensional, non-divergent velocity components from the faces of each “C” grid cell are linearly interpolated onto the particle’s position within the grid cell. For example, the eastward (along the x-axis) velocity of a particle is given by

$$u(x) = u_{i-1} + \frac{(x - x_{i-1})}{(x_i - x_{i-1})} (u_i - u_{i-1}), \quad (1)$$

where the subscripts $i - 1$ and i denote the western and eastern walls of the grid cell where the particle is located, respectively. This can be re-written as

$$\frac{\partial x}{\partial t} + \beta x + \delta = 0, \quad (2)$$

where $\beta = (u_i - u_{i-1})/\Delta x$ and $\delta = -u_{i-1} - \beta x_{i-1}$ (Döös et al., 2013). This differential equation can be solved analytically for $\beta \neq 0$ as

$$x_{t_1} = \left(x_0 + \frac{\delta}{\beta} \right) \exp^{-\beta(t_1 - t_0)} - \frac{\delta}{\beta} \quad (3)$$

269 The time it will take for the particle to reach the eastern or western face of the grid
 270 cell can be computed by taking $x_{t_1} = x_i$ or $x_{t_1} = x_{i-1}$, respectively, and solving for
 271 t_1 . For each advective timestep, the times required for the particle to reach any of the
 272 6 walls of the grid cell are computed using (3). If any of those times is shorter than
 273 the advective timestep, the particle is advected until it reaches the cell wall. Then the
 274 flow field in the adjacent grid cell is considered and the particle is advected over the
 275 remaining time.

276 **2.2.2 Particle Seeding**

277 For all particle-tracking experiments, a single particle seeding event is prescribed.
 278 In the horizontal, particles are seeded every 250 m over the entire domain in the x-
 279 direction, and for $100 < y < 200$ km in the y-direction. The seeding is centered over
 280 the mean position of the central front (see Figure 2) and is therefore not affected by
 281 undesired effects created by the solid north-south solid boundaries. In the vertical,
 282 particles are seeded every 1 m between 75 and 85 m. This depth range is chosen as it
 283 corresponds to the average euphotic depth at Station Papa, defined by the 1% light
 284 level. Particle seeding is located at the base of the euphotic layer where biological pro-
 285 cesses not captured by the particles (e.g., grazing, repackaging, aggregation, etc.) are
 286 not as active (Ducklow et al., 2001). The euphotic depth was computed for the months
 287 of February and June over the period 2007-2016 from profiles of Photosynthetically
 288 Active Radiation (PAR) collected at Station Papa as part of the long-term monitoring
 289 of Line P executed by the Department of Fisheries and Ocean Canada¹. The average
 290 euphotic depth computed for both of these months is around 80 m, which agrees with
 291 previously established estimates of the euphotic depth (Sherry et al., 1999; Harrison
 292 et al., 2004).

293 In each particle-tracking experiment, three different classes of particles are re-
 294 leased. Each particle class is characterized by a different sinking velocity: 0.025, 1,
 295 and 5 m/day. In this study, these particle classes are referred to as slow- intermediate-,
 296 and fast-sinking particles. This characterization is not based on the absolute value of
 297 the sinking rate, but rather on the ratio with vertical currents in the study region. The
 298 slowest-sinking class is essentially selected to represent non-sinking particles: based on
 299 the setup of our experiments, the slowest-sinking particles would take 400 days to sink
 300 10 m through gravitational sinking, a timescale much greater than commonly observed
 301 remineralization timescales. While 5 m/day remains a relatively slow sinking rate, this
 302 “fastest-sinking” velocity is chosen as an end-member velocity class of particle, based
 303 on the PDF of vertical velocities in the model. At any given time, at least 85% of
 304 the model vertical velocity is weaker than 5 m/day. The results presented for the 5
 305 m/day sinking class can therefore be theoretically extrapolated to any class with a
 306 higher sinking velocity.

307 The advective timestep for particles is set to 1.5 hours. The flow field is linearly
 308 interpolated in time between model outputs, justifying the higher temporal resolution
 309 used for particle tracking in *Papa_winter*. Particle positions are saved every 3 hours,
 310 along with key model variables interpolated onto the particle positions (e.g., density,
 311 vorticity). Particles are tracked for four weeks (28 days). Each particle-tracking ex-
 312 periment contains 1,971,717 particles per sinking-velocity class, for a total of 9,858,585

¹ <https://www.waterproperties.ca/linep/index.php>

313 particles. Particles located deeper than the maximum winter mixed layer (i.e., 100 m;
 314 Pelland et al., 2016; Plant et al., 2016) are considered exported, as they will likely not
 315 be re-entrained into the mixed layer.

316 **2.2.3 Density and Biomass Spectra**

To quantify vertical export fluxes, both the distribution of the number of particles and the associated biomass can be modeled based on two main variables: the particles' radii and the rate at which the number of particles changes with respect to the size. The particle number is modeled using a power-law function as a function of size that is driven by the parameter ξ . This slope ξ of the size spectrum of particles (also known as the Junge slope; White et al., 2015) is the slope of the log-log curve of particle number N vs. particle radius r , where

$$N(r) = N_0 \left(\frac{r}{r_0} \right)^{-\xi} . \quad (4)$$

317 Here, N_0 and r_0 represent a reference particle number and radius, chosen arbitrarily.
 318 Typical values for ξ derived from both in-situ observations and satellite data have been
 319 reported to range from 3 to 6 (Kostadinov et al., 2009; White et al., 2015). For small
 320 particles ($<400 \mu\text{m}$) and relatively low temperature ($<15^\circ\text{C}$), it has been shown that
 321 the relationship between particle radius r and sinking velocity w_s exhibits a range of
 322 variation and is difficult to determine empirically. Nevertheless, Stokes' law, where
 323 $w_s \propto r^2$, is often used as a lower-bound sinking velocity estimate (Bach et al., 2012).

Assuming a Stokes-like relationship, we can construct based on (4) a particle sinking velocity spectrum $N(w_s)$, as a function of the Junge slope ξ :

$$N(w_s) = N_0 \left(\frac{w_s}{w_{s_0}} \right)^{-\xi/2} , \quad (5)$$

324 where w_{s_0} is the sinking speed of particles with radius r_0 . For a specific slope and
 325 sinking-velocity class, an equivalent number of particles per simulated particle can be
 326 computed using (5) (See Figure 4). For example, using the largest sinking velocity
 327 class as a reference (i.e., $w_{s_0} = 5 \text{ m/day}$ and $N_0 = 1,971,717$), and a spectral slope
 328 $\xi = 4$, each simulated particle with a sinking velocity of 0.025 m/day in fact represents
 329 40,000 particles (Figure 4).

The relative biomass of a particle in a specific sinking-velocity class, $B_p(w_s)$ can be estimated if the biomass is assumed to scale with the particle's volume. The relative biomass of one particle in a sinking-velocity class w_s can therefore be computed as

$$B_p(w_s) = B_p(w_{s_0}) \left(\frac{w_s}{w_{s_0}} \right)^{3/2} \quad (6)$$

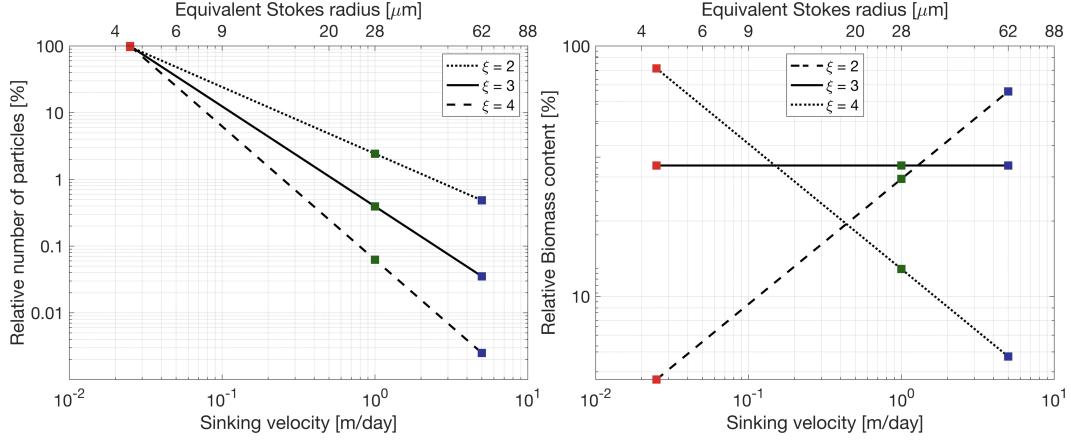
where $B_p(w_{s_0})$ is the biomass of a particle in the sinking velocity class w_{s_0} . The total biomass associated with one simulated particle can be obtained by scaling (6) by the ratio $N(w_s)/N_0$:

$$B(w_s) = B_0 \left(\frac{w_s}{w_{s_0}} \right)^{3/2} \frac{N(w_s)}{N_0} \quad (7)$$

where $B_0 = B_p(w_{s_0})$. Combining (5) and (7) yields an expression relating the biomass associated with a simulated particle for a specific sinking-velocity class and the spectral slope (Figure 4):

$$B(w_s) = B_0 \left(\frac{w_s}{w_{s_0}} \right)^{\frac{3-\xi}{2}} . \quad (8)$$

334 Using the same example as before where $\xi = 4$, if the amount of biomass associated
 335 with one simulated particle in the 5 m/day sinking-velocity class is taken as $B_0 = 1$,
 336 then one simulated particle sinking at 0.025 m/day contains 14.14 units of biomass



330 **Figure 4.** Relative number of particles (left) and biomass (right) as a function of sinking
 331 velocity w_s . Sinking velocity spectrum are shown for three different Junge slope ξ : 2 (dotted),
 332 3 (solid), and 2 (dashed). Colored squares indicate the sinking velocities of the three particle
 333 classes modeled: 0.025 m/day (red), 1 m/day (green), and 5 m/day (blue).

337 and a single particle contains $14.14/40,000 = 3.5 \times 10^{-4}$ units of biomass (see Figure
 338 4). This normalized formulation of particle number and biomass (see Equations (5)
 339 and (8)) has the advantage that the impact of spectral slope on the relative export of
 340 biomass can be quantified without needing a large number of particle-tracking exper-
 341 iments, where the number of seeded particles would vary to account for the different
 342 spectral slopes. For the purpose of this study, only the relative amount of biomass is
 343 relevant. For simplicity, we define a normalized biomass unit for $\xi = 3$ as $B_0 = 1$. The
 344 values taken by B_0 for other Junge slopes ξ are computed under the condition that
 345 the total amount of biomass is kept constant (Figure 4b).

346 2.2.4 Particle Remineralization Scheme

Remineralization of particles as they sink through the water column impacts the amount of biomass exported. Slow-sinking particles generally contain less biomass and spend more time in the mixed layer, which means that they are remineralized at a shallower depth than faster sinking particles. Remineralization processes are complex, species-dependent, and generally not well-understood. In the absence of a consensus on a general functional form of particle remineralization, we rely on an idealized relationship which assumes that the biomass content of a particle decreases in time proportionally to the particle volume. Remineralization is thus modeled as an exponential decrease of biomass with time at a rate k (Iversen & Ploug, 2010, 2013)

$$B(t) = B^0 \exp(-kt), \quad (9)$$

where B^0 denotes the biomass content at $t = 0$ days, and the remineralization rate is taken to be $k = 0.13 \text{ day}^{-1}$ in this study (Iversen & Ploug, 2010). This remineralization rate is independent of particle sinking velocity, and seems to lie within the range of other estimates (Ploug et al., 2008; Iversen & Ploug, 2010, 2013). The change in biomass with time is in turn expected to affect the sinking velocity of the particle. Given that $B \propto w^{3/2}$ (see Equation (6)), particles in all sinking-velocity classes undergo a decay in sinking speed according to

$$w_s(t) = w_s^0 \exp\left(-\frac{2kt}{3}\right), \quad (10)$$

where w_s^0 is the initial sinking velocity at $t = 0$ days. In this study, the impact of remineralization is thus considered through the implementation of a time-dependent sinking velocity (Equation 10). While particles classes are classified based on their initial sinking-velocity, it is worth noting that over the length of the particle-tracking experiments that include remineralization (28 days), particle sinking speeds slow down to 10% of their initial velocity.

3 Results

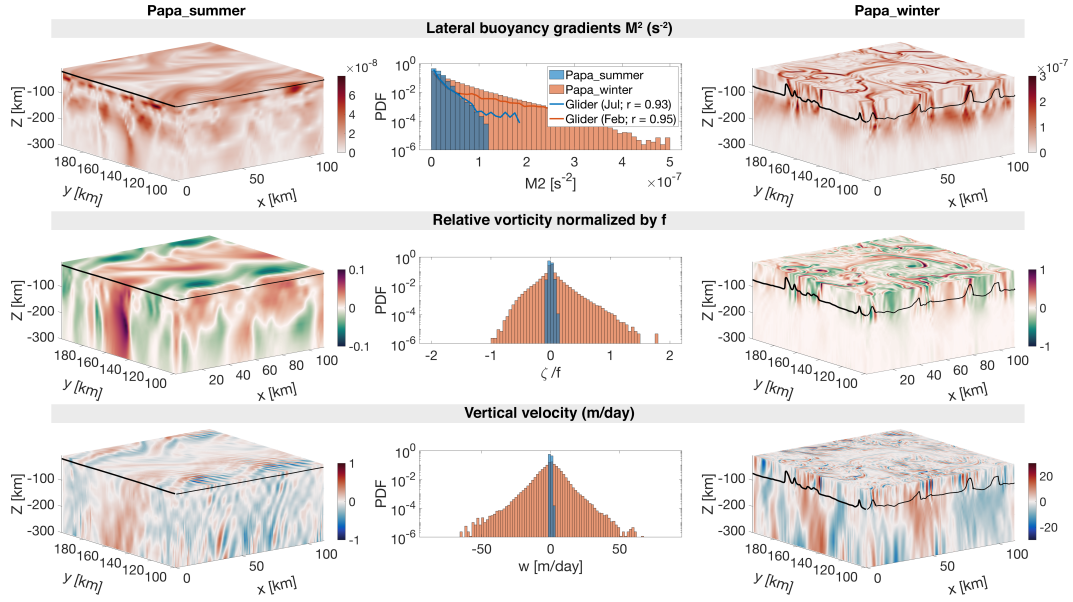
3.1 Seasonally varying dynamical regimes

Two model experiments are designed to capture different dynamical conditions observed in the Northeast Pacific Ocean in summer and winter. *Papa_summer* is initialized in early spring (doy 105) when the water column is characterized by a relatively deep mixed layer (~ 100 m) and a halocline located between 100 and 150 m (Figure 2). The forcing by a realistic, positive, net heat flux generates the restratification of the water column, with the development of a strong thermocline between 25 and 50 m leading to the shoaling of the mixed layer and a subsurface peak in N^2 at about 30 m (see Figure 2). A comparison between model outputs and monthly-averaged density profiles from underwater gliders collected in June and July over the period 2008-2009 yields correlation coefficients of $r = 0.87$ and $r = 0.88$, respectively. These high correlation suggest that *Papa_summer* numerical experiment captures the vertical spring and summer conditions in the Northeast Pacific Ocean.

In the horizontal, the prescribed density fronts progressively become unstable within the first 60 days of the experiment (Figure 2). During this time, the Total Kinetic Energy (KE_{tot}) contained in the model domain slowly increases before reaching a maximum at doay 162, where it remains relatively constant for the rest of the simulation. The flattening of the KE_{tot} curve is used to determine the time necessary for the simulation to spin-up, hence determining the start day of the particle-tracking experiments. The ocean dynamics associated with *Papa_summer* are characterized using PDFs of horizontal buoyancy gradients ($M^2 = |\nabla_H b|^2$), vertical velocities (w), and Rossby numbers computed from the normalized vertical component of the relative vorticity ($Ro = (v_x - u_y)/f$ where $f = 1.12 \times 10^{-4}$; Figure 5).

Lateral buoyancy gradients in the summer are relatively weak $\mathcal{O}(10^{-8} \text{ s}^{-2})$ and result in low Rossby numbers $\mathcal{O}(0.1)$, with positive relative vorticity on the denser (north) side of the front and negative relative vorticity on the lighter (south) side of the front. Corresponding vertical velocities are consistently weaker than 1 m/day ($< 10^{-5}$ m/s) and are characterized by regions of weak upwelling and downwelling on 10 km scales, associated with the meandering of the front (Bower & Rossby, 1989). Alternating bands of upwelling and downwelling at $\mathcal{O}(1 \text{ km})$ spatial scale are superimposed, and likely caused by propagating internal waves. Coherent vertical velocity structures extend to depths much greater than the mixed layer depth (~ 25 m; Figure 5). The amplitude of the vertical velocity field coincides with the expected order of magnitude given by the scaling $w \propto Ro f U / N$ (Mahadevan, 2016): using $Ro \sim 0.1$ (Figure 5), $N \sim 10^{-2} \text{ s}^{-1}$ (Figure 2), $f \sim 10^{-5} \text{ s}^{-1}$, and $U \sim 0.01 \text{ m/s}$, we obtain $w \sim 10^{-6} \text{ m/s}$, or $\sim 10^{-1} \text{ m/day}$.

Papa_winter is, on the other hand, initialized in the winter (doy 0) to capture a time period where the mixed layer depth is deeper (~ 100 m) and density gradients more pronounced (Pelland et al., 2016). At this time of year, the water column in this region is characterized by the presence of a deep halocline between 100 and 150 m (Figure 3 Pelland et al., 2016). After spin-up, the vertical stratification remains consistent throughout the model run, and compares well with the vertical profile obtained from glider observations for the month of March ($r = 0.95$; see Figure 3). In



377 **Figure 5.** Snapshots of M^2 (top), ζ/f (middle), and w (bottom) half-way through the partic-
 378 le tracking experiment for *Papa_summer* (left) and *Papa_winter* (right), with the Mixed Layer
 379 Depth indicated by the solid black line. The corresponding Probability Distribution Functions
 380 (PDFs) are shown in the center for both *Papa_summer* (blue) and *Papa_winter* (red). Note the
 381 different colorbars used for *Papa_summer* and *Papa_winter*. Histograms of M^2 computed from
 382 glider data at Station Papa in February (blue line) and July (red line) are superimposed in the
 383 top middle panel.

404 the horizontal, prescribed density fronts are much sharper than in summer (i.e., over
 405 smaller spatial scales $\mathcal{O}(1 \text{ km})$ vs. $\mathcal{O}(10 \text{ km})$). Because of these stronger density
 406 gradients, combined with the alternating zonal winds and constantly negative surface
 407 heat flux, the fronts become unstable more rapidly than in summer (Figure 3). As a
 408 result, KE_{tot} starts to plateau at day 48. The experiment is considered spun-up by
 409 day 50 and the particle-tracking experiment is initialized.

410 The frontal structures visible in the horizontal buoyancy gradient field are as-
 411 sociated with filaments of relatively high Rossby number of $\mathcal{O}(1)$ (Figure 5). The
 412 PDF of relative vorticity reveals a positively-skewed distribution ($s = 0.68$). This is in
 413 agreement with the fact that the relative vorticity is more likely to be cyclonic than an-
 414 ticyclonic, based on conservation of potential vorticity (Hoskins & Bretherton, 1972).
 415 Regions with high Rossby number are localized and located in the mixed layer exclu-
 416 sively. In places where the local Rossby number reaches $\mathcal{O}(1)$, geostrophic balance is
 417 lost and a vertical secondary ageostrophic circulation begins to slump the isopycnals
 418 and restore the flow to a more geostrophically-balanced flow. This ageostrophic sec-
 419 ondary circulation therefore generates “hot spots” of higher vertical velocities. The
 420 fine-scale structures in the vertical velocity field corresponding to $\mathcal{O}(1)$ Rossby num-
 421 bers can be seen in Figure 5, with local vertical velocities up to 60 m/day ($\sim 7 \times 10^{-4}$
 422 m/s). Contrary to the PDF of relative vorticity, the distribution of vertical velocities
 423 demonstrate a negative skewness ($s = -0.25$). This is in agreement with the theory:
 424 In fact, positive relative vorticity is associated with the dense side of a density front,
 425 where vertical velocities are negative (Mahadevan, 2016). Once again, the amplitude
 426 of these vertical velocity hot spots is coherent with the scaling $w \propto \text{Ro}fU/N$: using

427 $Ro \sim 1$, $N \sim 10^{-2}$ 1/s, $f \sim 10^{-5}$ 1/s, and $U \sim 0.1$ m/s, we obtain $w \sim 10^{-4}$ m/s, or
 428 $\sim 10^1$ m/day.

429 Comparing *Papa_summer* and *Papa_winter* highlights the different dynamical
 430 regimes in the two experiments. In *Papa_winter*, density fronts tend to be sharper,
 431 meaning larger density gradients over shorter spatial scales. When computed at the
 432 kilometer-scale, the PDF of horizontal buoyancy gradients in *Papa_winter* exhibits a
 433 longer tail than in *Papa_summer* (Figure 5). When compared to observations, the
 434 PDFs of M^2 in *Papa_summer* and *Papa_winter* demonstrate a correlation with obser-
 435 vations of $r = 0.93$ and $r = 0.95$, respectively.

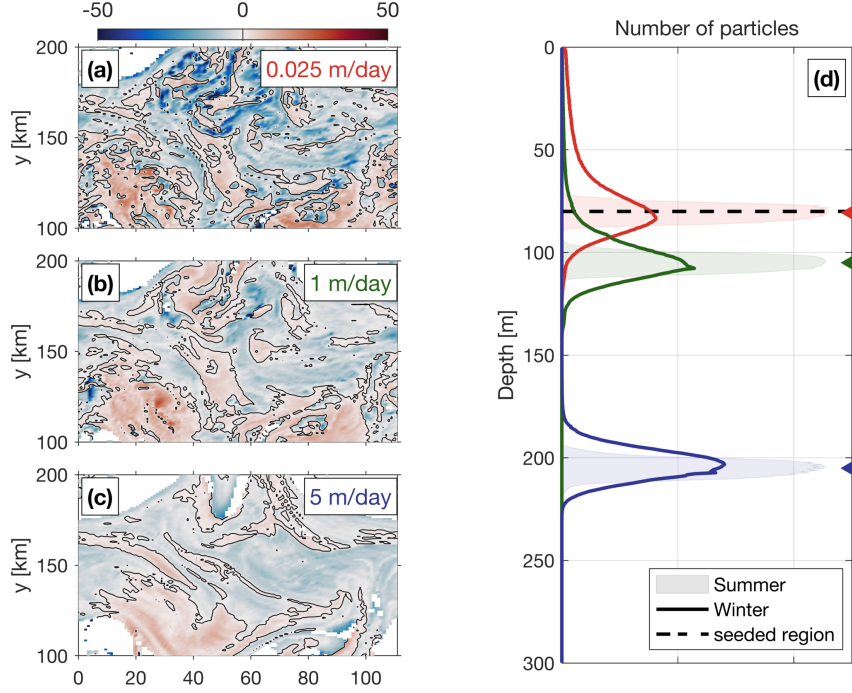
436 The wider PDF of vertical velocities in *Papa_winter* shows advective velocities
 437 that match and exceed typical gravitational sinking velocities, particularly for smaller,
 438 and therefore slower-sinking, particulate organic material. The secondary ageostrophic
 439 circulation that develops at submeso-scales (i.e., $Ro \sim O(1)$) therefore generates an ex-
 440 port mechanism that directly competes with the traditional paradigm that relies on
 441 gravitational sinking leading the export of particulate matter in the ocean.

442 3.2 Gravitational and Advective Export of POC

443 Both model experiments described above were then used to investigate the re-
 444 lationship between ocean dynamics and particle downward flux, using Lagrangian
 445 particle-tracking. Domain-averaged, downward particle flux is expected to be a com-
 446 bination of the flux driving by gravitational sinking ($\langle w_s B \rangle$), and by the vertical ad-
 447 vective currents affecting the particle along its pathway ($\langle w B \rangle$). The deviation in
 448 particle depths from the traditional one-dimensional gravitationally driven model is
 449 shown in Figure 6 for both summer and winter cases. In the summer, the PDF of par-
 450 ticle density versus depth remains relatively narrow through time, and is centered on
 451 a depth level that can be predicted using a simple 1D gravitational model (see shaded
 452 curves in Figure 6). The spread in the particle density also vary little among particle
 453 classes with different sinking velocities, suggesting that downward fluxes of particles
 454 is greatly dominated by gravitational settling and is not subject to significant vertical
 455 ocean currents.

467 In the winter, however, PDFs of particle density versus depth is wider, in agree-
 468 ment with the stronger vertical ocean currents occurring in the winter (see Figure 5).
 469 A top-view of the deviation in the downward particle flux from the traditionally con-
 470 sidered 1D gravitational model can be seen in Figure 6 (panels (a)-(c)). Slower-sinking
 471 particles deviate more than faster-sinking particles, exhibiting median depth anom-
 472 alies up to 50 m. This is due to the fact that slower-sinking particles spend more time
 473 in the mixed layer, where most of the stronger vertical currents tend to occur (Figure
 474 5). An interesting result emerges from the spatial distribution of the depth-anomaly:
 475 both positive (i.e., particles are shallower than expected) and negative (i.e., particles
 476 are deeper than expected) anomalies are organized into features with a length-scale
 477 $\mathcal{O}(1-10$ km). This further highlights the importance of winter submesoscale circulation
 478 for vertical fluxes of particles.

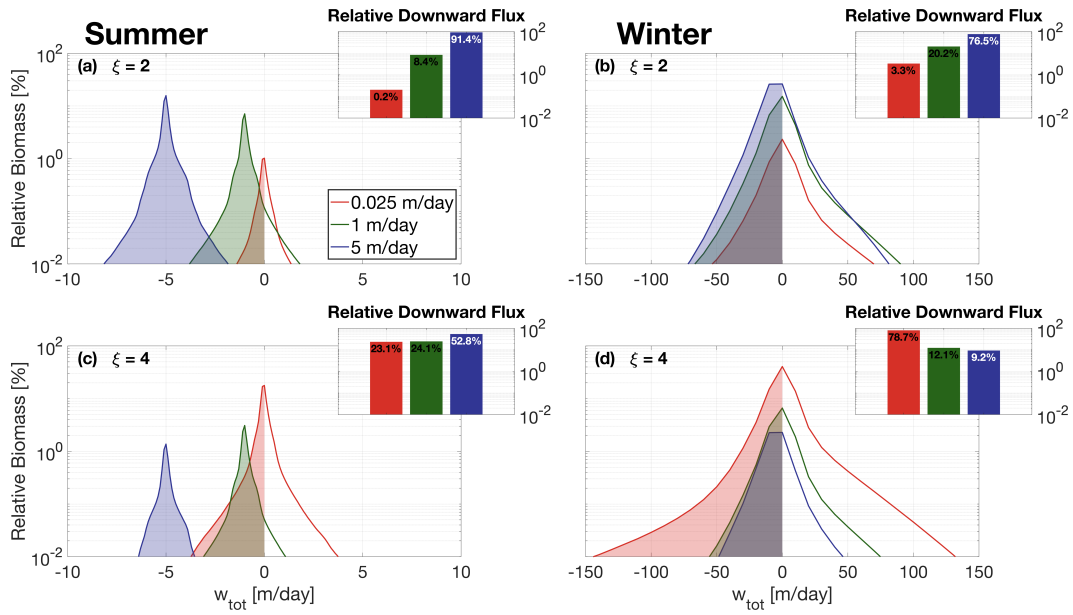
479 A relative amount of biomass is associated to the particles using Equation (8).
 480 PDFs of relative biomass as a function of the vertical velocity is shown in Figure 7.
 481 Following the traditional paradigm derived from the simple 1D gravitational model, the
 482 downward flux of biomass in the summer is dominated by faster-sinking particle classes
 483 capable of carrying particulate material downwards more efficiently. The contribution
 484 of slower-sinking particles, however, depends critically on the slope of the size spectrum
 485 (see Figure 4). As the Junge slope increases, the spectrum of biomass steepens, and
 486 the relative contribution of slower-sinking particles to the downward biomass flux
 487 significantly increases (Figure 7c). In fact, the contribution of slower-sinking particles
 488 to the summer downward flux increases by a factor 100 (from 0.2% to 0%) when the



456 **Figure 6.** [left] The median depth anomaly of particles with a sinking speed (a) 0.025 m/d,
 457 (b) 1 m/d, (c) 5 m/d within each grid cell for the winter case 25 days after particles are released.
 458 The ‘depth anomaly’ is with respect to the ‘expected’ sinking depth (= sinking speed \times time
 459 since release). Blue (red) grid cells indicate that the median depth of particles in this cell is
 460 deeper (shallower) than expected, based on a 1D gravitational model where $z = w_s \times t$. [right] (d)
 461 Probability Distribution Function (PDF) of particles as a function of depth for each velocity class
 462 (red = 0.025 m/day; green = 1 m/day; blue = 5 m/day). The winter distribution is shown as
 463 thick lines, while the summer distribution is represented by the shaded regions. Triangle markers
 464 indicate the expected depth of particles after 25 days based on the 1D gravitational model, which
 465 is used as a reference to compute the depth anomalies. Release depth is indicated by the thick
 466 dashed line.

489 Junge slope varies from $\xi = 2$ to $\xi = 4$. While significant, the impact of a change in
 490 the Junge slope in summer conditions does not challenge the dominant role played by
 491 faster-sinking particles. This result can be explained by the fact that, in the summer,
 492 vertical velocities are weak and vertical biomass fluxes are therefore gravitationally-
 493 driven ($\langle w_s B \rangle > \langle w B \rangle$).

501 In the winter, PDFs of relative biomass as a function of vertical velocities present
 502 a much larger spread, with velocity magnitudes exceeding 50 m/day. For $\xi = 2$,
 503 the relative contribution of slower-sinking particles to the downward flux significantly
 504 increases from 0.2% in the summer to about 3% in the winter, demonstrating the
 505 impact advective velocities alone can have on vertical fluxes (Figure 7b). Nevertheless,
 506 slower-sinking particles remain a relatively small contributor to the total downward
 507 flux of biomass. When winter ocean dynamics are coupled with a steeper Junge slope,
 508 however, slower-sinking particles largely dominate the downward biomass flux. In
 509 our winter simulations with $\xi = 4$, we find that the slowest-sinking particle class is
 510 responsible for about 79% of the biomass flux (Figure 7d).

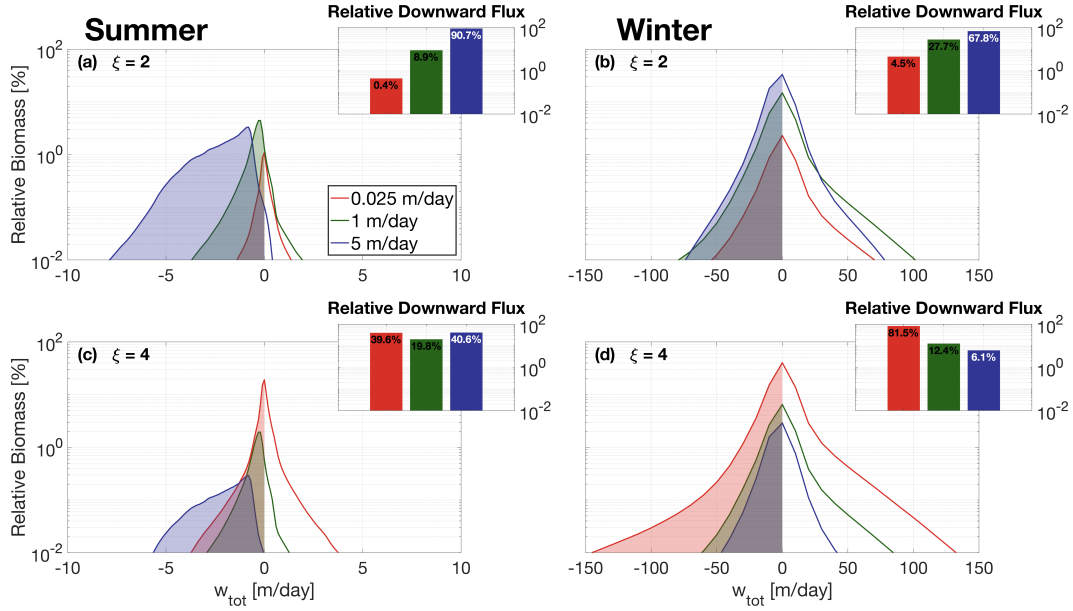


494 **Figure 7.** Probability Distribution Function (PDF) of relative biomass versus total vertical
 495 velocity (sinking + advective) along particle trajectories in the summer case [left] and winter case
 496 [right], with a Junge slope of 2 [top] and 4 [bottom]. PDFs are computed from the whole 24-day
 497 particle tracking experiments. Inserts show the integrated relative downward biomass flux asso-
 498 ciated with each sinking-velocity class, categorized according to their initial sinking velocity (red
 499 = 0.025 m/day; green = 1 m/day; blue = 5 m/day). Both winter dynamics and steeper Junge
 500 slopes tend to increase the relative contribution of slower-sinking particles.

511 Our results show that both a steepening of the particle size spectrum and the
 512 presence of submesoscale dynamics can enhance the contribution of slower-sinking parti-
 513 cles to the downward biomass flux. While the former is simply due to an increase in
 514 particle density in slower-sinking particle classes, the latter is attributed to the larger
 515 vertical velocity generated by submesoscale instabilities. When both are combined,
 516 as expected in the wintertime, slower-sinking particles then become the leading con-
 517 tributor to the downward biomass transport. However, slower-sinking particles are
 518 generally expected to remineralize on timescales shorter than their export timescale,
 519 fueling the argument that the focus should be upon faster-sinking particle classes. The
 520 impacts of remineralization on export are thus considered in the following section to
 521 test the robustness of the findings.

522 3.3 Particle Remineralization

523 Both submesoscale dynamics and the Junge slope were identified as key factors
 524 impacting the respective role played by different particle classes in driving downward
 525 biomass fluxes. Simple Lagrangian particles were used to isolate the effects of these
 526 two factors. In reality, however, sinking velocities of particulate matter varies in time
 527 as the particles slowly remineralize. A remineralizing behavior was therefore imple-
 528 mented for the Lagrangian particles, using Equation (10), to investigate the impact
 529 that remineralization processes have on our findings. The traditional paradigm relies
 530 on the fact that slow-sinking particles tend to fully remineralize over short timescales,
 531 further enhancing the importance of faster-sinking particles classes in driving down-
 532 ward biomass fluxes. While this paradigm holds for flatter Junge slope, where the



547 **Figure 8.** Same as Figure 7, but including particle remineralization (see Equation 10).

533 biomass content is dominated by faster-sinking particles, it becomes unfit at steeper
 534 slopes.

535 Figure 8 compares the relative biomass and downward biomass fluxes associated
 536 with each of the modeled particle classes for $\xi = 2$ and $\xi = 4$ including the remineralization
 537 scheme. As previously detailed, downward fluxes of biomass are dominated by
 538 faster-sinking particles during summertime and in the absence of remineralization (see
 539 Figure 7). This is due to the fact that the flux of biomass $\langle w_{tot}B \rangle = \langle w_sB \rangle + \langle wB \rangle$
 540 is driven by $\langle w_sB \rangle$, despite a smaller relative biomass content per particle. This is
 541 characteristic of a gravitationally-driven system, where settling velocity dictates the
 542 contribution to downward fluxes. Implementing remineralization processes, however,
 543 directly affects the particle settling velocity which slows down as particles remineralize.
 544 This effect can particularly be seen in Figure 8a and c, where PDFs of relative biomass
 545 per particle class are shifted towards weaker vertical velocities than in the absence of
 546 remineralization, as predicted by Equation (10).

548 In an advectively-driven system where $\langle w_sB \rangle \sim \langle wB \rangle$, the relative amount of
 549 biomass content in a particle class becomes important and dictates the respective
 550 contribution of each particle class to the total downward biomass fluxes. This shift from a
 551 gravitationally-driven to an advectively-driven system is observed when implementing
 552 particle remineralization in the summer (Figure 8): in the absence of remineralization,
 553 faster-sinking particles dominate the downward biomass fluxes (53%; see Figure 7c).
 554 When remineralization processes are considered, slower-sinking particles contribute
 555 more to biomass fluxes (see inset in Figure 8c). As shown in Figure 7, downward
 556 biomass fluxes in the wintertime are generally advectively-driven, due to the larger
 557 vertical velocities associated with wintertime ocean dynamics. Biomass fluxes are
 558 dominated by the slower-sinking particles when $\xi = 4$, representing 79% of the down-
 559 ward biomass flux (Figure 7d). Even after implementing the remineralization scheme,
 560 slower-sinking particles remain the largest contributor to downward biomass fluxes
 561 (82%; see Figure 8d).

562 These results highlight the importance in considering slower-sinking particle
 563 classes when considering downward biomass fluxes. It also demonstrates that, con-
 564 trarily to the traditional paradigm, remineralization processes enhance the role played
 565 by slower-sinking particles in biomass fluxes, in cases where the biomass spectrum
 566 slope is negative.

567 4 Discussion

568 4.1 Dynamical Regimes

569 *Papa_summer* and *Papa_winter* experiments were designed to statistically cap-
 570 ture the ocean dynamics at Station Papa (145°W, 50°N) in the Northeast Pacific
 571 Ocean. After spin-up, the model demonstrated similar distributions of both horizontal
 572 (M^2) and vertical (N^2) density gradients to observational estimates from underwater
 573 gliders (see Figures 2, 3, and 5). The two experiments, however, show significantly
 574 different distributions of M^2 , with the winter distribution exhibiting a longer tail, due
 575 to sharper density gradients. The tail of the wintertime distribution is only partially
 576 captured by the glider data, due to the fact that underwater gliders sampled gradients
 577 at spatial scales of 10 km and greater, while the model has a horizontal resolution of
 578 500 m, allowing sharper submesoscale fronts and filaments to be formed.

579 Studies investigating submesoscale dynamics traditionally focused on regions
 580 where the presence of submesoscale fronts and filaments are established, such as west-
 581 ern boundary currents with strong gradients (D’Asaro et al., 2011; Thomas, Tandon, &
 582 Mahadevan, 2013), or the edge of mesoscale features (van Haren et al., 2006; Waite et
 583 al., 2016). The seasonality in submesoscale dynamics captured in the glider dataset at
 584 Station Papa and reflected in the model experiments, echoes the behavior seen from
 585 recent observational studies conducted at a similar latitude in the Atlantic Ocean,
 586 which demonstrate the intensification of submesoscale dynamics in the wintertime
 587 (Thompson et al., 2016; Buckingham et al., 2016). Despite being sometimes qualified
 588 as an “eddy desert” with low kinetic energy (Chelton et al., 2011), ocean characteristics
 589 in the eastern part of the Pacific subpolar gyre suggest the presence of submesoscale
 590 features in the wintertime: strong density gradients, localized Rossby numbers of order
 591 1, a balanced Richardson number $Ri_b = \frac{f^2 N^2}{M^4}$ smaller than 1, a positively skewed
 592 distribution in vorticity, and a negatively skewed distribution of vertical velocities (see
 593 Figure 5; Thomas, Taylor, et al., 2013; Rudnick, 2001; Buckingham et al., 2016).

594 Strong downward velocities are hypothesized to enhance POC export by advect-
 595 ing slower-sinking particles out of the mixed layer. *Papa_winter* indeed exhibits vertical
 596 velocities more than 20 times larger than in *Papa_summer*. The vertical currents in
 597 *Papa_winter*, however, tend to be much patchier than the weaker vertical currents
 598 observed in *Papa_summer*. Because both particle production and downward vertical
 599 velocities present a high degree of patchiness, it requires a certain level of covariance
 600 between the two fields for the export to effectively be enhanced (Mahadevan et al.,
 601 2012). A more realistic seeding strategy for Lagrangian particles, such as one guided
 602 by biological tracers, would likely provide important information towards a better
 603 understanding of the effects of patchiness on POC export at submeso-scales

604 The hypothesis tested in this study is that submesoscale activity enhances export
 605 of particulate matter at Station Papa by shortening the export timescale of particulate
 606 matter. The wintertime intensification in submesoscale activity has the potential to
 607 indeed enhance export (see discussion in Section 4.2). However, the seasonal cycle
 608 in submesoscale activity is out of phase with the one in net community productivity,
 609 which peaks in the spring and summertime when the mixed layer is shallower (Plant
 610 et al., 2016). Two mechanisms are therefore present to potentially sustain a year-long
 611 POC export flux: In the winter, less particulate material is present in the mixed layer,

612 but active submesoscale dynamics tend to enhance the POC export flux by advecting
 613 the more numerous slower-sinking particles into the ocean interior. In the summer,
 614 the production of POC is at its yearly maximum, but export tends to be dominated
 615 by gravitational sinking, which favors faster-sinking particles and thus exclude part of
 616 the particle spectrum from contributing to the export flux.

617 4.2 Downward Fluxes

618 Analyses of particle tracking experiments reveal that the contribution of slower-
 619 sinking particles to the downward particulate flux depends on two main factors: (1)
 620 the dynamics of the oceanic flow field, and (2) the slope of the size spectrum (i.e., the
 621 Junge slope ξ).

622 Mixed layer ocean dynamics at station Papa change significantly between the
 623 winter and the summer. In the winter, submesoscale dynamics are intensified, and
 624 sharp fronts and filaments develop in the mixed layer. This seasonal change in dy-
 625 namics is consistent with recent observations (Thompson et al., 2016; Buckingham et
 626 al., 2016), and models (Brannigan et al., 2015; Callies et al., 2015; Rocha et al., 2016)
 627 characterizing the seasonal cycle of submesoscale dynamics. The winter intensification
 628 in submesoscale dynamics was proven to have an important impact on the downward
 629 flux of all sinking-velocity classes modeled in this experiment.

630 In the summer, gravitational sinking governs a downward particulate flux, which
 631 is dominated by faster-sinking particles, with little to no contribution from slower-
 632 sinking particles. In the winter, however, vertical fluxes tend to be advectively-driven,
 633 which leads to a slightly weaker downward flux of faster-sinking particles than in the
 634 summer due to resuspension, but a much larger flux of slower-sinking particles, which
 635 are present in far greater numbers (Figure 7). The gravitationally-driven flux in the
 636 summer is mechanistically different from the advectively-driven winter flux, which
 637 raises the question as to which process is most efficient in driving a downward flux of
 638 particulate material.

639 In the absence of remineralization, both a steeper size spectrum slope ($\xi > 3$ in
 640 this case) and enhanced submesoscale dynamics, increase the contribution of slower-
 641 sinking particle classes to the downward biomass flux. This is only when both of these
 642 conditions are combined, however, that slower-sinking particles dominate the down-
 643 ward flux of biomass (Figure 7). This is a significant result, as Junge slopes greater
 644 than 3 have been observed in the ocean : In-situ observations yield average spectral
 645 slopes varying between 3.5 and 4.5 (see Table 2 in Kostadinov et al., 2009), while
 646 spectral analysis of satellite data suggest global spectral slopes varying between 3 and
 647 6. More recent observational work located in the Northeast Pacific, including Station
 648 Papa, found a spectral slope also greater than 3(White et al., 2015). Junge slopes are
 649 expected to vary in space, depending on the community composition, both laterally
 650 and vertically (Kostadinov et al., 2009; White et al., 2015), as well as in time; spec-
 651 trum slopes tend to be flatter during a spring bloom event, where larger particles (e.g.,
 652 diatoms) are produced in large quantities, and steeper during the wintertime, when
 653 communities are mostly composed of small particles (Parsons & Lalli, 1988; Dale et
 654 al., 1999; Behrenfeld, 2010). The threshold value of $\xi = 3$ for a change in the biomass
 655 spectral slope (see Figure 4b) is of course a consequence of first-order approximations
 656 used in this study describing the relationships between particle size, sinking veloci-
 657 ty, and biomass content. Nevertheless, our results demonstrate the importance of
 658 including the smaller particle size range of the particle spectrum, in the estimation or
 659 measurement of vertical fluxes, especially when submesoscale dynamics are active. It
 660 also highlights the importance of better constraining the relationships linking particle
 661 size, sinking velocity, and biomass content.

662 Introducing remineralization processes significantly decreases the biomass flux.
 663 Counter-intuitively, however, the implementation of a remineralization scheme further
 664 strengthens the contribution of slower-sinking particles to the biomass flux (Figure
 665 8). This can be explained by the fact that remineralization processes have a greater
 666 impact on sinking-velocity classes that rely on gravitational sinking to be exported, as
 667 these particles decelerate as they remineralize. In the summer, all particle classes are
 668 similarly affected by remineralization, as downward fluxes are gravitationally-driven.
 669 In the winter, however, slower-sinking particles are exported through advective pro-
 670 cesses. Their export timescale is barely affected by remineralization processes as it
 671 only depends on local ocean dynamics.

672 These results are robust to the range of sinking rates explored. If one considers a
 673 particle class with a sinking rate far exceeding the vertical advective velocity (e.g., 100
 674 m/day; Turner, 2015), then the associated biomass flux can be estimated by relying
 675 on the traditional 1-D paradigm, assuming $w_{tot} \approx w_s$. Combining this approximation
 676 with Equation 8 shows that the slope of the biomass flux spectrum is positive for
 677 $\xi < 5$, in which case very fast-sinking particles would dominate vertical biomass fluxes.
 678 However, for $\xi > 5$, the slope of the biomass flux spectrum becomes negative as
 679 well, meaning that the biomass flux is always dominated by the slow-sinking particle
 680 classes, regardless of the ocean dynamical regime. While considered large, values of
 681 $\xi > 5$ remain realistic and fall within the range obtained from satellite-based estimates
 682 (Kostadinov et al., 2009).

683 The results of this study suggest that slow- and non-sinking particles must be
 684 considered when studying the downward flux of particulate matter in the upper ocean.
 685 The patchiness associated with both particle production and submesoscale features
 686 poses a real observational challenge to properly resolve vertical fluxes. Based on our
 687 findings, subsequent studies should focus on testing the impact of patchiness on vertical
 688 fluxes. In the wintertime, when size spectral slope is steep and submesoscale dynamics
 689 most active, vertical fluxes could be grossly underestimated depending on the level of
 690 co-occurrence between particle production and stronger vertical currents.

691 5 Conclusion

692 The main conclusions of this study are:

- 693 1. Ocean dynamics in the subpolar Northeast Pacific exhibit a seasonal cycle with
 694 low submesoscale activity in the summertime, and more submesoscale features
 695 present in the wintertime. Submesoscale dynamics generate larger, and asym-
 696 metric, vertical currents leading to a vertical biomass flux driven by advective
 697 processes, as opposed to gravitational sinking in the summertime.
- 698 2. Submesoscale dynamics generally enhance the downward particulate flux by
 699 increasing the contribution of slower-sinking particles to the total flux through
 700 advective transport. The slower-sinking particles are found to be significant
 701 for export, and can be even make the dominant contribution under certain
 702 conditions.
- 703 3. The contribution of slower-sinking particles to the downward biomass flux de-
 704 pends on the slope of the particle size spectra (i.e., the Junge Slope), that
 705 controls the relative number of particles per size class. Two cases emerge from
 706 this study:
 - 707 (a) If the Junge slope is smaller than 3, larger particles contribute most to vertical
 708 biomass fluxes independently of flow dynamics, as there are no mechanisms
 709 capable of selectively advecting slower-sinking particles. The system is de-
 710 scribed as gravitationally-driven.

- 711 (b) If the Junge slope is greater than 3, as most commonly observed, ocean
 712 dynamics become key for determining which particle classes dominate the
 713 downward flux. As submesoscale dynamics become more active, ageostrophic
 714 circulations leading to larger vertical velocities develop. In these conditions,
 715 downward biomass fluxes are largely driven by the slower-sinking particle
 716 classes.
- 717 4. Remineralization processes logically reduce the amount of biomass flux. How-
 718 ever, it unexpectedly enhances the role of slower-sinking particles, which are
 719 advectively transported. The impact of remineralization is greater on faster-
 720 sinking particles since it affects both the biomass content and their sinking
 721 velocity.

722 Acknowledgments

723 The work was funded by NASA grant NNX16AR48G, to complement the EXport
 724 Processes in the global Ocean from RemoTe Sensing (EXPORTS) program. We would
 725 like to thank A. Thompson (Caltech) for his useful comments and suggestions, N.
 726 Pelland (NOAA) and C. Eriksen (University of Washington) for sharing the glider data
 727 collected at Ocean Station Papa, as well as S. Essink for his assistance in developing the
 728 particle-tracking code. All data used in this manuscript are publicly available: Ocean
 729 Station Papa data is available on PMEL’s website ([https://www.pmel.noaa.gov/](https://www.pmel.noaa.gov/ocs/Papa)
 730 [ocs/Papa](https://www.pmel.noaa.gov/ocs/Papa); PMEL, 2018) and gridded Argo products can be downloaded at [http://](http://www.seanoe.org/data/00348/45945)
 731 www.seanoe.org/data/00348/45945 (Gaillard, 2015). Glider data is archived at the
 732 University of Washington’s Library (<http://hdl.handle.net/1773/41656>; Pelland,
 733 2018). Code to reproduce analysis and figures are publicly available at [https://](https://github.com/matdever/Size-differentiated_Export_GBC)
 734 github.com/matdever/Size-differentiated_Export_GBC (Dever, 2020). Due to the
 735 very large filesize, model outputs and particle trajectories are available on request.

736 References

- 737 Alkire, M., D’Asaro, E., Lee, C., Perry, M., Gray, A., Cetinic, I., . . . González-
 738 Posada, A. (2012). Estimates of net community production and export using
 739 high-resolution, Lagrangian measurements of O₂, NO₃⁻, and POC through the
 740 evolution of a spring diatom bloom in the North Atlantic. *Deep-Sea Res. I*, *64*,
 741 157-174. doi: 10.1016/j.dsr.2012.01.012
- 742 Armstrong, R. A., Lee, C., Hedges, J. I., Honjo, S., & Wakeham, S. G. (2001). A
 743 new, mechanistic model for organic carbon fluxes in the ocean based on the
 744 quantitative association of POC with ballast minerals. *Deep Sea Research Part*
 745 *II*, *49*(1), 219-236. doi: 10.1016/S0967-0645(01)00101-1
- 746 Bach, L. T., Riebesell, U., Sett, S., Febiri, S., Rzepka, P., & Schulz, K. G. (2012).
 747 An approach for particle sinking velocity measurements in the 3–400 μm size
 748 range and considerations on the effect of temperature on sinking rates. *Marine*
 749 *Biology*, *159*(8), 1853–1864. doi: 10.1007/s00227-012-1945-2
- 750 Baker, C. A., Henson, S. A., Cavan, E. L., Giering, S. L., Yool, A., Gehlen, M., . . .
 751 Sanders, R. (2017). Slow-sinking particulate organic carbon in the atlantic
 752 ocean: Magnitude, flux, and potential controls. *Global Biogeochemical Cycles*,
 753 *31*(7), 1051-1065. doi: 10.1002/2017GB005638
- 754 Behrenfeld, M. J. (2010). Abandoning sverdrup’s critical depth hypothesis on phyto-
 755 plankton blooms. *Ecology*, *91*(4), 977-989. doi: 10.1890/09-1207.1
- 756 Bower, A. S., & Rossby, T. (1989). Evidence of Cross-Frontal Exchange Processes in
 757 the Gulf Stream Based on Isopycnal RAFOS Float Data. *Journal of Physical*
 758 *Oceanography*, *19*(9), 1177–1190. doi: 10.1175/1520-0485(1989)019<1177:
 759 EOCFEP>2.0.CO;2
- 760 Brannigan, L., Marshall, D. P., Naveira-Garabato, A., & George Nurser, A. (2015).
 761 The seasonal cycle of submesoscale flows. *Ocean Modelling*, *92*, 69–84. doi: 10

- 762 .1016/j.ocemod.2015.05.002
- 763 Briggs, N., Perry, M. J., Cetinić, I., Lee, C., D'Asaro, E., Gray, A. M., & Rehm, E.
764 (2011). High-resolution observations of aggregate flux during a sub-polar north
765 atlantic spring bloom. Deep Sea Research Part I: Oceanographic Research
766 Papers, 58(10), 1031 - 1039. doi: 10.1016/j.dsr.2011.07.007
- 767 Buckingham, C. E., Naveira Garabato, A. C., Thompson, A. F., Brannigan, L.,
768 Lazar, A., Marshall, D. P., ... Belcher, S. E. (2016). Seasonality of sub-
769 mesoscale flows in the ocean surface boundary layer. Geophysical Research
770 Letters, 43(5), 2118–2126. doi: 10.1002/2016GL068009
- 771 Callies, J., Ferrari, R., Klymak, J. M., & Gula, J. (2015). Seasonality in sub-
772 mesoscale turbulence. Nature communications, 6, 6862. doi: 10.1038/
773 ncomms7862
- 774 Chelton, D. B., Schlax, M. G., & Samelson, R. M. (2011). Global observations of
775 nonlinear mesoscale eddies. Progress in Oceanography, 91(2), 167–216. doi: 10
776 .1016/j.pocean.2011.01.002
- 777 Dale, T., Rey, F., & Heimdal, B. R. (1999). Seasonal development of phytoplankton
778 at a high latitude oceanic site. Sarsia, 84(5-6), 419-435. doi: 10.1080/00364827
779 .1999.10807347
- 780 D'Asaro, E., Lee, C., Rainville, L., Harcourt, R., & Thomas, L. (2011). Enhanced
781 turbulence and energy dissipation at ocean fronts. Science, 332(6027), 318–322.
782 doi: 10.1126/science.1201515
- 783 Dever, M. (2020). Size differentiated Export GBC: Release 1. (data retrived from
784 GitHub, https://github.com/matdever/Size-differentiated_Export_GBC)
785 doi: 10.5281/zenodo.3908126
- 786 DeVries, T., Liang, J.-H., & Deutsch, C. (2014). A mechanistic particle flux model
787 applied to the oceanic phosphorus cycle. Biogeosciences, 11(19), 5381-5398.
788 doi: 10.5194/bg-11-5381-2014
- 789 Döös, K., Kjellsson, J., & Jönsson, B. (2013). TRACMASS – A Lagrangian Trajec-
790 tory Model. In Preventive methods for coastal protection (pp. 225–249). Hei-
791 delberg: Springer International Publishing. doi: 10.1007/978-3-319-00440-2_7
- 792 Ducklow, H. W., Steinberg, D. K., & Buesseler, K. O. (2001). Upper Ocean Carbon
793 Export and the Biological Pump. Oceanography, 14. doi: [https://doi.org/10](https://doi.org/10.5670/oceanog.2001.06)
794 .5670/oceanog.2001.06
- 795 Estapa, M. L., Siegel, D. A., Buesseler, K. O., Stanley, R. H. R., Lomas, M. W., &
796 Nelson, N. B. (2015). Decoupling of net community and export production
797 on submesoscales in the Sargasso Sea. Global Biogeochemical Cycles, 29(8),
798 1266–1282. doi: 10.1002/2014GB004913
- 799 Falkowski, P. G., Barber, R. T., & Smetacek, V. (1998). Biogeochemical Controls
800 and Feedbacks on Ocean Primary Production. Science, 281(5374), 200–206.
801 doi: 10.1126/science.281.5374.200
- 802 Fox-Kemper, B., Ferrari, R., & Hallberg, R. (2008). Parameterization of
803 Mixed Layer Eddies. Part I: Theory and Diagnosis. Journal of Physical
804 Oceanography, 38(6), 1145–1165. doi: 10.1175/2007JPO3792.1
- 805 Gaillard, F. (2015). ISAS-13 temperature and salinity gridded fields. SEANOE. doi:
806 10.17882/45945
- 807 Gaillard, F., Reynaud, T., Thierry, V., Kolodziejczyk, N., & von Schuckmann, K.
808 (2016). In situ-based reanalysis of the global ocean temperature and salinity
809 with isas: Variability of the heat content and steric height. Journal of Climate,
810 29(4), 1305-1323. doi: 10.1175/JCLI-D-15-0028.1
- 811 Gruber, N., Lachkar, Z., Frenzel, H., Marchesiello, P., Münnich, M., McWilliams,
812 J. C., ... Plattner, G.-K. (2011). Eddy-induced reduction of biological produc-
813 tion in eastern boundary upwelling systems. Nature geoscience, 4(11), 787. doi:
814 10.1038/NCEO1273
- 815 Harrison, P. J., Whitney, F. A., Tsuda, A., Saito, H., & Tadokoro, K. (2004).
816 Nutrient and Plankton Dynamics in the NE and NW Gyres of the Sub-

- 817 arctic Pacific Ocean. *Journal of Oceanography*, 60(1), 93–117. doi:
818 10.1023/B:JOCE.0000038321.57391.2a
- 819 Hoskins, B. J., & Bretherton, F. P. (1972). Atmospheric Frontogenesis Models:
820 Mathematical Formulation and Solution. *Journal of the Atmospheric Sciences*,
821 29(1), 11–37. doi: 10.1175/1520-0469(1972)029<0011:AFMMFA>2.0.CO;2
- 822 Iversen, M. H., & Ploug, H. (2010). Ballast minerals and the sinking carbon flux in
823 the ocean: carbon-specific respiration rates and sinking velocity of marine snow
824 aggregates. *Biogeosciences*, 7(9), 2613–2624. doi: 10.5194/bg-7-2613-2010
- 825 Iversen, M. H., & Ploug, H. (2013). Temperature effects on carbon-specific respi-
826 ration rate and sinking velocity of diatom aggregates - potential implications
827 for deep ocean export processes. *Biogeosciences*, 10(6), 4073–4085. doi:
828 10.5194/bg-10-4073-2013
- 829 Jackson, G. A., Maffione, R., Costello, D. K., Alldredge, A. L., Logan, B. E., &
830 Dam, H. G. (1997). Particle size spectra between 1 μm and 1 cm at Monterey
831 Bay determined using multiple instruments. *Deep Sea Research Part I*, 44(11),
832 1739–1767. doi: 10.1016/S0967-0637(97)00029-0
- 833 Klein, P., & Lapeyre, G. (2009). The Oceanic Vertical Pump Induced by Mesoscale
834 and Submesoscale Turbulence. *Annual Review of Marine Science*, 1(1), 351–
835 375. doi: 10.1146/annurev.marine.010908.163704
- 836 Kostadinov, T. S., Siegel, D. A., & Maritorena, S. (2009). Retrieval of the particle
837 size distribution from satellite ocean color observations. *Journal of Geophysical*
838 *Research*, 114(C9), C09015. doi: 10.1029/2009JC005303
- 839 Lévy, M., Ferrari, R., Franks, P. J. S., Martin, A. P., & Rivière, P. (2012). Bringing
840 physics to life at the submesoscale. *Geophysical Research Letters*, 39(14), n/a–
841 n/a. doi: 10.1029/2012GL052756
- 842 Lévy, M., Klein, P., & Treguier, A.-M. (2001). Impact of sub-mesoscale physics
843 on production and subduction of phytoplankton in an oligotrophic regime.
844 *Journal of marine research*, 59(4), 535–565. doi: 10.1357/002224001762842181
- 845 Mahadevan, A. (2016). The Impact of Submesoscale Physics on Primary Product-
846 tivity of Plankton. *Annual Review of Marine Science*, 8(1), 161–184. doi: 10
847 .1146/annurev-marine-010814-015912
- 848 Mahadevan, A., & Archer, D. (2000). Modeling the impact of fronts and
849 mesoscale circulation on the nutrient supply and biogeochemistry of the up-
850 per ocean. *Journal of Geophysical Research: Oceans*, 105(C1), 1209–1225. doi:
851 10.1029/1999JC900216
- 852 Mahadevan, A., D’Asaro, E., Lee, C., & Perry, M. J. (2012). Eddy-Driven Strat-
853 ification Initiates North Atlantic Spring Phytoplankton Blooms. *Science*,
854 337(6090), 54–58. doi: 10.1126/science.1218740
- 855 Mahadevan, A., Oliger, J., & Street, R. (1996a). A Nonhydrostatic Mesoscale Ocean
856 Model. Part II: Numerical Implementation. *Journal of Physical Oceanography*,
857 26(9), 1881–1900. doi: 10.1175/1520-0485(1996)026<1881:ANMOMP>2.0.CO;2
- 858 Mahadevan, A., Oliger, J., & Street, R. (1996b). A Nonhydrostatic mesoscale ocean
859 model. Part I: Well-posedness and scaling. *Journal of Physical Oceanography*,
860 26(9), 1868–1880. doi: 10.1175/1520-0485(1996)026<1868:ANMOMP>2.0.CO;2
- 861 Mahadevan, A., & Tandon, A. (2006). An analysis of mechanisms for submesoscale
862 vertical motion at ocean fronts. *Ocean Modelling*, 14(3-4), 241–256. doi: 10
863 .1016/J.OCEMOD.2006.05.006
- 864 McCave, I. (1984). Size spectra and aggregation of suspended particles in the deep
865 ocean. *Deep Sea Research Part I*, 31(4), 329–352. doi: 10.1016/0198-0149(84)
866 90088-8
- 867 McDonnell, A., & Buesseler, K. (2012). A new method for the estimation of sinking
868 particle fluxes from measurements of the particle size distribution, average
869 sinking velocity, and carbon content. *Limnology and Oceanography: Methods*,
870 10, 329–346. doi: 10.4319/lom.2012.10.329
- 871 McDonnell, A. M. P., & Buesseler, K. O. (2010). Variability in the average sinking

- 872 velocity of marine particles. *Limnology and Oceanography*, 55(5), 2085–2096.
873 doi: 10.4319/lo.2010.55.5.2085
- 874 McWilliams, J. C. (2016). Submesoscale currents in the ocean. *Proceedings of the*
875 *Royal Society A: Mathematical, Physical and Engineering Science*, 472(2189).
876 doi: 10.1098/rspa.2016.0117
- 877 Mensa, J. A., Garraffo, Z., Griffa, A., Özgökmen, T. M., Haza, A., & Veneziani, M.
878 (2013). Seasonality of the submesoscale dynamics in the Gulf Stream region.
879 *Ocean Dynamics*, 63(8), 923–941. doi: 10.1007/s10236-013-0633-1
- 880 Mesinger, F., DiMego, G., Kalnay, E., Mitchell, K., Shafran, P. C., Ebisuzaki,
881 W., . . . Shi, W. (2006). North american regional reanalysis. *Bulletin*
882 *of the American Meteorological Society*, 87(3), 343-360. doi: 10.1175/
883 BAMS-87-3-343
- 884 Omand, M. M., D’Asaro, E. A., Lee, C. M., Perry, M. J., Briggs, N., Cetini, I.,
885 & Mahadevan, A. (2015). Eddy-driven subduction exports particulate
886 organic carbon from the spring bloom. *Science*, 348(6231), 222–225. doi:
887 10.1126/science.1260062
- 888 Omand, M. M., Govindarajan, R., He, J., & Mahadevan, A. (2020). Sinking flux of
889 particulate organic matter in the oceans: Sensitivity to particle characteristics.
890 *Scientific reports*, 10(1), 1–16. doi: 10.1038/s41598-020-60424-5
- 891 Parsons, T. R., & Lalli, C. M. (1988). Comparative oceanic ecology of the plankton
892 communities of the subarctic Atlantic and Pacific oceans. *Oceanography and*
893 *Marine Biology Annual Review*, 26, 317–359.
- 894 Pelland, N. (2018). Seaglider Surveys at Ocean Station Papa: Bin-Averaged Profiles, Currents, and Independent C
895 Retrieved from <http://hdl.handle.net/1773/41656>
- 896 Pelland, N., Eriksen, C., & Cronin, M. (2016). Seaglider surveys at Ocean Station
897 Papa: Circulation and watermass properties in a meander of the North Pa-
898 cific Current. *Journal of Geophysical Research: Oceans*, 121, 6816–6846. doi:
899 10.1002/2016JC011920
- 900 Petrik, C., Jackson, G., & Checkley, D. (2013). Aggregates and their distributions
901 determined from LOPC observations made using an autonomous profiling
902 float. *Deep Sea Research Part I*, 74, 64-81. doi: 10.1016/j.dsr.2012.12.009
- 903 Plant, J. N., Johnson, K. S., Sakamoto, C. M., Jannasch, H. W., Coletti, L. J.,
904 Riser, S. C., & Swift, D. D. (2016). Net community production at Ocean Sta-
905 tion Papa observed with nitrate and oxygen sensors on profiling floats. *Global*
906 *Biogeochemical Cycles*, 30(6), 859–879. doi: 10.1002/2015GB005349
- 907 Ploug, H., Iversen, M. H., Koski, M., & Buitenhuis, E. T. (2008). Production,
908 oxygen respiration rates, and sinking velocity of copepod fecal pellets: Direct
909 measurements of ballasting by opal and calcite. *Limnology and Oceanography*,
910 53(2), 469–476. doi: 10.4319/lo.2008.53.2.0469
- 911 PMEL. (2018). Pacific Marine Environment Laboratory Ocean Climate Stations Mooring Data.
912 Retrieved from <https://www.pmel.noaa.gov/ocs/data-overview>
- 913 Richardson, T., & Jackson, G. (2007). Small phytoplankton and carbon export from
914 the surface ocean. *Science*, 315, 838-840. doi: 10.1126/science.1133471
- 915 Riley, J., Sanders, R., Marsay, C., Le Moigne, F. A., Achterberg, E. P., & Poul-
916 ton, A. J. (2012). The relative contribution of fast and slow sinking parti-
917 cles to ocean carbon export. *Global Biogeochemical Cycles*, 26(1). doi:
918 10.1029/2011GB004085
- 919 Rocha, C. B., Gille, S. T., Chereskin, T. K., & Menemenlis, D. (2016). Seasonal-
920 ity of submesoscale dynamics in the Kuroshio Extension. *Geophysical Research*
921 *Letters*, 43(21), 11,304–11,311. doi: 10.1002/2016GL071349
- 922 Rudnick, D. L. (2001). On the skewness of vorticity in the upper ocean. *Geophysical*
923 *Research Letters*, 28(10), 2045–2048. doi: 10.1029/2000GL012265
- 924 Sheldon, R., Prakash, A., & Sutcliffe, W., Jr. (1972). The size distribution of parti-
925 cles in the ocean. *Limnology and Oceanography*, 17(3), 327-340. doi: 10.4319/
926 lo.1972.17.3.0327

- 927 Sherry, N. D., Boyd, P. W., Sugimoto, K., & Harrison, P. J. (1999). Seasonal and
928 spatial patterns of heterotrophic bacterial production, respiration, and biomass
929 in the subarctic NE Pacific. *Deep-Sea Research Part II: Topical Studies in*
930 *Oceanography*, 46(11-12), 2557–2578. doi: 10.1016/S0967-0645(99)00076-4
- 931 Stukel, M. R., Aluwihare, L. I., Barbeau, K. A., Chekalyuk, A. M., Goericke, R.,
932 Miller, A. J., ... others (2017). Mesoscale ocean fronts enhance carbon ex-
933 port due to gravitational sinking and subduction. *Proceedings of the National*
934 *Academy of Sciences*, 114(6), 1252–1257. doi: 10.1073/pnas.1609435114
- 935 Taylor, J. R., Smith, K. M., & Vreugdenhil, C. A. (2020). The influence of submes-
936 oscales and vertical mixing on the export of sinking tracers in large-eddy
937 simulations. *Journal of Physical Oceanography*, 50(5), 1319–1339. doi:
938 10.1175/JPO-D-19-0267.1
- 939 Thomas, L. N., Tandon, A., & Mahadevan, A. (2013). Submesoscale processes and
940 dynamics. In *Ocean modeling in an eddying regime* (p. 17–38). American Geo-
941 physical Union (AGU). doi: 10.1029/177GM04
- 942 Thomas, L. N., Taylor, J. R., Ferrari, R., & Joyce, T. M. (2013). Symmetric in-
943 stability in the Gulf Stream. *Deep Sea Research Part II: Topical Studies in*
944 *Oceanography*, 91, 96–110. doi: 10.1016/j.dsr2.2013.02.025
- 945 Thompson, A. F., Lazar, A., Buckingham, C., Naveira Garabato, A. C., Damerell,
946 G. M., & Heywood, K. J. (2016). Open-Ocean Submesoscale Motions: A Full
947 Seasonal Cycle of Mixed Layer Instabilities from Gliders. *Journal of Physical*
948 *Oceanography*, 46(4), 1285–1307. doi: 10.1175/JPO-D-15-0170.1
- 949 Turner, J. T. (2015). Zooplankton fecal pellets, marine snow, phytodetritus and the
950 ocean’s biological pump. *Progress in Oceanography*, 130, 205–248.
- 951 van Haren, H., Millot, C., & Taupier-Letage, I. (2006). Fast deep sinking in Mediter-
952 ranean eddies. *Geophysical Research Letters*, 33(4), L04606. doi: 10.1029/
953 2005GL025367
- 954 Waite, A. M., Stemmann, L., Guidi, L., Calil, P. H. R., Hogg, A. M. C., Feng, M.,
955 ... Gorsky, G. (2016). The wineglass effect shapes particle export to the deep
956 ocean in mesoscale eddies. *Geophysical Research Letters*, 43(18), 9791–9800.
957 doi: 10.1002/2015GL066463
- 958 White, A. E., Letelier, R. M., Whitmire, A. L., Barone, B., Bidigare, R. R., Church,
959 M. J., & Karl, D. M. (2015). Phenology of particle size distributions
960 and primary productivity in the North Pacific subtropical gyre (Station
961 ALOHA). *Journal of Geophysical Research: Oceans*, 120(11), 7381–7399.
962 doi: 10.1002/2015JC010897